9

Raman Lidar

Ulla Wandinger

Leibniz Institute for Tropospheric Research,
Permoserstraße 15, D-04318 Leipzig, Germany (ulla@tropos.de)

9.1 Introduction

The Raman lidar technique makes use of the weak inelastic scattering of light by atmospheric molecules [1–8]. The excitation of a variety of rotational and vibrational molecular energy levels leads to several bands of Raman scattered radiation the frequency shifts of which are characteristic for the interacting molecule. Raman lidar systems have become widely used instruments in atmospheric research during the past decade [9–16]. The very robust technique makes low demands concerning spectral purity of the emitted laser light and frequency stabilization of the receiver. However, it suffers from the low cross sections of Raman scattering and thus from the comparably small signal-to-noise ratios of the measurements. For a long time, Raman lidar instruments were therefore mainly used at nighttime. Daytime applications increased with the development of high-power transmitters and narrow-bandwidth detection systems which allow a sufficient suppression of the daylight background [11, 17–19].

Raman measurements do not require specific laser wavelengths as it is the case in the differential-absorption lidar (DIAL) technique (see Chapters 7 and 8). Because of the wavelength dependence of the Raman scattering cross section which is proportional to λ^{-4}, with λ denoting the wavelength of the laser light, shorter emission wavelengths are to be preferred. Attenuation of the laser light by gaseous, especially ozone, absorption can be avoided if wavelengths $\geq$320 nm are chosen. However, the solar-blind region below 300 nm has also been used for Raman measurements to avoid daylight background [20–29]. The signal attenuation by ozone absorption limits the range of these measurements to a few

kilometers. Concerning measurement range, laser wavelengths between 320 and 550 nm are best suited for Raman applications. In the visible spectral region, the higher atmospheric transmission, i.e., the lower signal extinction by Rayleigh scattering which is also proportional to λ^{-4}, partly compensates for the lower Raman scattering cross sections.

The low Raman scattering cross sections require comparably high concentrations of the investigated atmospheric components. Accordingly, nitrogen, oxygen, and water vapor as main constituent gases in air are of prime interest. Whereas nitrogen and oxygen, the atmospheric concentrations of which are known in principle from temperature and pressure, serve as reference gases, the water-vapor concentration is a major unknown in atmospheric studies and therefore a principal subject of Raman lidar investigations. For that reason, this chapter will mainly focus on Raman observations of atmospheric moisture. Several attempts have been made to measure other gaseous constituents of the atmosphere. Carbon dioxide [9, 30] and atmospheric pollutants such as sulfur dioxide [30, 31] and methane [32, 33] have been investigated. However, the detection limits necessary to allow the application of the technique in routine atmospheric monitoring are hard to reach and the achievable measurement ranges are low. One of the topics which gained further interest in recent years is the detection of Raman scattering from liquid water in tropospheric clouds [34–36].

Several Raman lidar applications are based on the measurement of profiles of the reference gases nitrogen and oxygen. The temperature dependence of the rotational Raman bands of these gases permits one to determine atmospheric temperature profiles from the ground up to about 40 km height [5, 19, 37–41]. This technique is further explained in Chapter 10. The measurement of extinction and backscatter coefficients and thus of the extinction-to-backscatter ratio, or lidar ratio, of aerosols and optically thin clouds makes use of the fact that the Raman backscatter coefficient of the reference gas is known and the lidar equation can therefore be solved for the unknown particle extinction coefficient [42, 43]. The wide field of research based on this technique is discussed in Chapter 4. Two Raman nitrogen and/or oxygen signals, one of which is partly absorbed by ozone, are used to determine ozone concentrations using the so-called Raman DIAL technique [44–46].

Table 9.1 gives an overview of the Raman lidar techniques and their typical achievable measurement ranges under consideration of the latest technical developments. The use of the rotational Raman (RR) and vibration—rotation Raman bands (VRR) is discussed in more detail below.

Table 9.1. Overview of Raman lidar techniques. VRR – vibration–rotation Raman band, RR – rotational Raman band, SB – solar-blind spectral region

Measured quantity	Interacting molecule, Raman band used	Typical achievable measurement range
Water-vapor mixing ratio	H_2O (vapor), VRR (+ reference gas, VRR)	0–12 km (night) [16, 47] 0–5 km (day) [11, 47]
Extinction coefficient Backscatter coefficient Lidar ratio	N_2 or O_2, VRR or RR (+ elastic signal for back-scatter and lidar ratio)	0–30 km (night) [48] 0–10 km (day) [49]
Temperature	N_2 and/or O_2, RR	0–40 km (night) [19, 40] 0–12 km (day) [19]
Ozone concentration (Raman DIAL)	N_2 and/or O_2, VRR-VRR or RR-VRR	3–20 km (night) [46] 0–3 km (day SB) [29]
Other trace-gas concentrations	Specific gas, VRR (+ reference gas, VRR)	0–1 km (day and night) [32]
Liquid water	H_2O (liquid), VRR (+ reference gas, VRR)	0–4 km (night) [34]

In the following Section 9.2, the basic principles of Raman scattering are explained. Section 9.3 describes technical requirements and principal features of a Raman lidar system. The determination of water-vapor profiles and their errors is discussed in Section 9.4. Section 9.5 briefly introduces the Raman ozone DIAL technique and the measurement of liquid water. Finally, a few concluding remarks are given in Section 9.6.

9.2 Basic Principles of Raman Scattering

9.2.1 Frequency Shifts

The scattering of incident radiation by atmospheric molecules involves elastic and inelastic processes. We speak of elastic or Rayleigh scattering if the frequency of the scattered photon $\tilde{\nu}_s$ is the same as the frequency of the incident photon $\tilde{\nu}_1$. In this case the molecule preserves its vibration–rotation energy level during the scattering process. Inelastic or Raman scattering processes lead to a change of the molecule's quantum state, and the frequency of the scattered photon is shifted by an amount $|\Delta\tilde{\nu}|$ [50–52]. If the molecule absorbs energy, i.e., a higher energy level is excited, the frequency of the scattered photon is decreased, $\tilde{\nu}_s = \tilde{\nu}_1 - |\Delta\tilde{\nu}|$, the wavelength is red-shifted. We call this inelastic process Stokes Raman scattering. If the molecule transfers energy to the scattered photon by decreasing its energy level, the frequency of the scattered photon is

increased, $\tilde{\nu}_s = \tilde{\nu}_l + |\Delta\tilde{\nu}|$, the wavelength is blue-shifted, and we speak of anti-Stokes Raman scattering. The shift

$$\Delta\tilde{\nu} = \tilde{\nu}_l - \tilde{\nu}_s = \frac{\Delta E}{hc_0} \tag{9.1}$$

is characteristic for the scattering molecule. Here ΔE is the energy difference between the molecular energy levels involved, h is Planck's constant, and c_0 the speed of light in vacuum. (For the sake of consistency with the spectroscopic literature, we use the wavenumber $\tilde{\nu} = 1/\lambda$ and the wavenumber shift $\Delta\tilde{\nu}$ both with the unit cm^{-1} to describe the frequency and frequency shift of radiation. We follow, as far as possible, the recent book by D.A. Long [53] which we recommend for further reading.)

The calculation of molecular energy levels is straightforward for homonuclear diatomic molecules, in our case N_2 and O_2 [53–57]. For such molecules the approximation with the model of a freely rotating harmonic oscillator gives the energy of the vibrational levels:

$$E_{\mathrm{vib},v} = hc_0\tilde{\nu}_{\mathrm{vib}}(v + 1/2), \quad v = 0, 1, 2, \ldots , \tag{9.2}$$

with the specific vibrational wavenumber or oscillator frequency of the molecule $\tilde{\nu}_{\mathrm{vib}}$ and the vibrational quantum number v.

For the rotational energy levels we get in a good approximation

$$E_{\mathrm{rot},J,v} = hc_0[B_v J(J+1) - D_v J^2(J+1)^2], \quad J = 0, 1, 2, \ldots . \tag{9.3}$$

J is the rotational quantum number, i.e., a series of rotational quantum levels belongs to each vibrational level. B_v is the specific rotational constant and D_v the centrifugal distortion or stretching constant of the molecule. The constants B_v and D_v depend on the actual vibrational state v of the molecule. The term with D_v considers the centrifugal stretching of the molecule's axis because of rotation. Its relative contribution to $E_{\mathrm{rot},J,v}$ is small and plays a role only for high J [57]. The molecular constants $\tilde{\nu}_{\mathrm{vib}}$, B_0, B_1, and D_0 needed to calculate Raman frequency shifts of N_2 and O_2 for Raman lidar applications are given in Table 9.2 [56–61].

A certain vibration–rotation energy level of the molecule is calculated from the sum of Eqs. (9.2) and (9.3). When applying these equations for the calculation of frequency shifts $\Delta\tilde{\nu}$ after Eq. (9.1), we have to consider the selection rules for vibrational and rotational transitions, which are

$$\Delta v = 0, \pm 1 \text{ and } \Delta J = 0, \pm 2, \tag{9.4}$$

Table 9.2. Molecular constants for the calculation of Raman frequency shifts of nitrogen and oxygen. The values for $\tilde{\nu}_{\mathrm{vib}}$ consider an anharmonicity correction for the transition from the ground state to the first excited vibrational state (see Ref. [53], p. 125 and 182)

Gas	$\tilde{\nu}_{\mathrm{vib}}$ cm^{-1}	B_0 cm^{-1}	B_1 cm^{-1}	D_0 cm^{-1}
N_2	2330.7	1.98957 [59]	1.97219 [59]	5.76×10^{-6} [59]
O_2	1556.4	1.43768 [58]	1.42188 [61]	4.85×10^{-6} [58]

with $\Delta J = J' - J''$. Here J' is the quantum number of the higher and J'' the one of the lower energy level involved in the transition, independent of which of the levels is the initial or the final one. In contrast, Δv is the difference of the vibrational quantum numbers of the final and the initial vibrational states.

Figure 9.1 depicts schematically the transitions between different vibration–rotation energy levels of the N_2 molecule and the resulting Raman spectrum. The transitions with $\Delta v = 0$ and $\Delta J = 0$ correspond to Rayleigh scattering. Transitions with $\Delta v = +1$ lead to the Stokes vibration–rotation band, and those with $\Delta v = -1$ to the anti-Stokes vibration–rotation band. If the rotational quantum number does not change during the vibrational transition, i.e., $\Delta J = 0$, the resulting Raman lines have very small frequency shifts between each other which are usually not resolved in lidar applications, and the group of lines is called the Q branch. Changes of $\Delta J = +2$ and $\Delta J = -2$ lead to the S and O branches, respectively. The rotational branches to the sides of the Rayleigh line are both of S type, since $J' > J''$ if $\Delta v = 0$. We call these lines the Stokes and anti-Stokes (pure) rotational Raman lines. From Eqs. (9.3) and (9.4) and by neglecting the centrifugal stretching, we obtain that the rotational Raman lines are equidistant. The first line is shifted from $\tilde{\nu}_1$ by $6B_0$, the next lines follow in distances of $4B_0$.

9.2.2 Cross Sections

The intensity of an observed Rayleigh or Raman line depends on the cross section of the corresponding vibration–rotation scattering process which is the product of the transition probability and the population of the initial energy level. For lidar applications we need the differential cross section $\mathrm{d}\sigma(\pi)/\mathrm{d}\Omega$ for scattering at 180°, which we call the backscatter

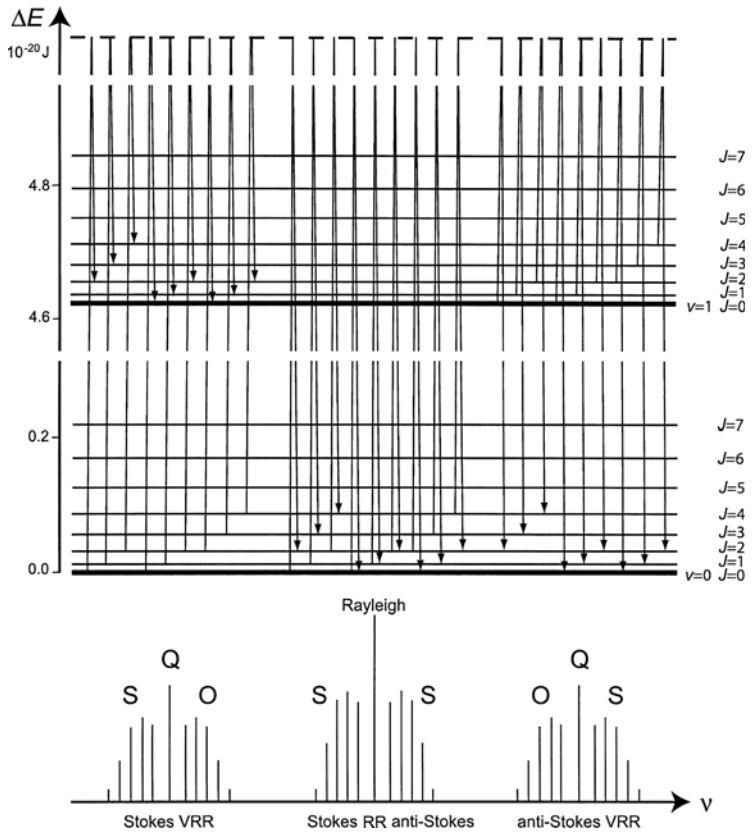

Fig. 9.1. Vibration–rotation energy levels of the N_2 molecule, Raman transitions, and resulting spectrum.

cross section. Cross sections are calculated from Placzek's polarizability theory [52] under the conditions that:

1) the frequency of the incident radiation is much larger than the frequency of any vibration–rotation transition of the molecule,
2) the frequency of the incident radiation is much smaller than any electronic transition frequency of the molecule,
3) the ground electronic state of the molecule is not degenerate.

These conditions, which exclude resonant scattering processes, are well satisfied for typical laser frequencies used in lidar and for the atmospheric molecules of interest.

The characteristic molecular parameters that determine the cross sections of a diatomic molecule are the mean polarizability a and the anisotropy of the polarizability γ and their derivatives with respect to the normal coordinate of vibration at the equilibrium position, a' and γ'. a^2 and γ^2 are invariants of the molecule's polarizability tensor. The derivatives a' and γ' characterize the change of the polarizability properties with changing distance between the atoms during vibration. From these parameters we get the differential cross section for Rayleigh backscattering,

$$\left(\frac{\mathrm{d}\sigma}{\mathrm{d}\Omega}\right)_{\mathrm{Ray}} = k_{\tilde{\nu}}\tilde{\nu}_1^4\left(a^2 + \frac{7}{180}\gamma^2\right), \tag{9.5}$$

the differential cross section for pure rotational Raman backscattering,

$$\left(\frac{\mathrm{d}\sigma}{\mathrm{d}\Omega}\right)_{\mathrm{RR}} = k_{\tilde{\nu}}\tilde{\nu}_1^4\left(\frac{7}{60}\gamma^2\right), \tag{9.6}$$

the differential cross section for Stokes vibration–rotation Raman backscattering,

$$\left(\frac{\mathrm{d}\sigma}{\mathrm{d}\Omega}\right)_{\mathrm{VRR}}^{\mathrm{Stokes}} = k_{\tilde{\nu}}(\tilde{\nu}_1 - \tilde{\nu}_{\mathrm{vib}})^4 \frac{b_v^2}{[1 - \exp(-hc_0\tilde{\nu}_{\mathrm{vib}}/k_{\mathrm{B}}T)]} \times \left(a'^2 + \frac{7}{45}\gamma'^2\right), \tag{9.7}$$

and the differential cross section for anti-Stokes vibration–rotation Raman backscattering,

$$\left(\frac{\mathrm{d}\sigma}{\mathrm{d}\Omega}\right)_{\mathrm{VRR}}^{\mathrm{anti\text{-}Stokes}} = k_{\tilde{\nu}}(\tilde{\nu}_1 + \tilde{\nu}_{\mathrm{vib}})^4 \frac{b_v^2}{[\exp(hc_0\tilde{\nu}_{\mathrm{vib}}/k_{\mathrm{B}}T) - 1]} \times \left(a'^2 + \frac{7}{45}\gamma'^2\right), \tag{9.8}$$

with the square of the zero-point amplitude of the vibrational mode

$$b_v^2 = \frac{h}{8\pi^2 c_0 \tilde{\nu}_{\mathrm{vib}}}, \tag{9.9}$$

and

$$k_{\tilde{\nu}} = \frac{\pi^2}{\epsilon_0^2}, \tag{9.10}$$

with the permittivity of vacuum ϵ_0. There are several remarks to be made in conjunction with these equations.

1) The cross sections in the given form hold for an assembly of molecules. Under atmospheric conditions, most of the molecules will be in their vibrational ground state with quantum number $v = 0$. However, there will be some population of higher vibrational energy levels with $v = 1, 2, \ldots$. The fraction of molecules in each vibrational state is calculated from the actual absolute temperature T after the Boltzmann distribution law with the Boltzmann constant k_B. In this way, we obtain the terms with the exponential function in square brackets in Eqs. (9.7) and (9.8) for the vibration–rotation transitions. From the ratio of these equations the intensity ratio of Stokes to anti-Stokes vibration–rotation Raman scattering is obtained as

$$\frac{(\mathrm{d}\sigma/\mathrm{d}\Omega)_{\mathrm{VRR}}^{\mathrm{Stokes}}}{(\mathrm{d}\sigma/\mathrm{d}\Omega)_{\mathrm{VRR}}^{\mathrm{anti\text{-}Stokes}}} = \frac{(\tilde{\nu}_1 - \tilde{\nu}_{\mathrm{vib}})^4}{(\tilde{\nu}_1 + \tilde{\nu}_{\mathrm{vib}})^4} \exp(hc_0\tilde{\nu}_{\mathrm{vib}}/k_\mathrm{B}T). \tag{9.11}$$

From this equation, we see that under atmospheric conditions the anti-Stokes vibration–rotation Raman bands have 3–6 orders less intensity than the corresponding Stokes bands. In a similar way, we can calculate the intensity ratios between Rayleigh and Raman scattered radiation or between rotational and vibration–rotation Raman scattered radiation from Eqs. (9.5)–(9.8).

2) Equations (9.5)–(9.8) hold for linearly polarized or unpolarized incident light and the polarization-independent observation of the complete backscatter signal. The equations can be transferred to other polarization configurations with the help of the Reference Tables of Ref. [53], the Central Reference Section of Ref. [55], or Ref. [62].

3) Equations (9.6)–(9.8) give the backscatter cross sections for the complete rotational and vibration–rotation Raman bands. The contributions from the different branches are obtained by appropriate separation of the last terms in Eqs. (9.5)–(9.8), i.e.,

$$\left(\frac{\mathrm{d}\sigma}{\mathrm{d}\Omega}\right)^{\mathrm{center}} \sim \left(a_l^2 + \frac{7}{180}\gamma_l^2\right) \text{ and } \left(\frac{\mathrm{d}\sigma}{\mathrm{d}\Omega}\right)^{\mathrm{wings}} \sim \left(\frac{7}{60}\gamma_l^2\right), \tag{9.12}$$

with $a_l^2 = a^2, a'^2$ and $\gamma_l^2 = \gamma^2, \gamma'^2$. The superscript *center* stands for either the Rayleigh line or the Q branch whereas *wings* describes the rotational side bands (O and S branches, see Fig. 9.1). We now see the equivalence between Rayleigh and rotational Raman scattering, on the one hand, and vibration–rotation Raman scattering, on the other hand.

Often the sum of Eqs. (9.5) and (9.6) is given as Rayleigh backscatter cross section, i.e., the contribution of rotational Raman scattering is added to the so-called Cabannes line [Eq. (9.5), $\Delta v = 0$, $\Delta J = 0$] and both together are referred to as Rayleigh scattering. Such a definition makes sense if the backscatter signal is detected with low spectral resolution, so that the rotational Raman lines contribute to the elastic backscatter signal measured with lidar.

4) If we want to calculate intensities of single Raman lines within the different branches, we need the population distribution for the initial rotational energy levels. Because the energy difference between the rotational levels is much smaller than between the vibrational levels, higher rotational energy levels of the vibrational ground state are well populated under atmospheric conditions. The population distribution follows again from the Boltzmann distribution law. In addition, we have to consider the degeneracy $2J + 1$ of the initial rotational energy level J, the nuclear-spin degeneracy $2I + 1$, and the nuclear-spin statistical weight factor g_N. The differential backscatter cross section for single lines can then be written as

$$\left(\frac{\mathrm{d}\sigma}{\mathrm{d}\Omega}\right)_J^{\mathrm{RR,VRR}} = k_{\tilde{\nu}}(\tilde{\nu}_1 \mp |\Delta\tilde{\nu}|)^4 \frac{g_N \Phi_J}{Q} \exp\left[-\frac{B_i h c_0 J(J+1)}{k_B T}\right], \tag{9.13}$$

with the actual frequency shift of the line $|\Delta\tilde{\nu}|$. B_i is the rotational constant of the initial vibrational state, i.e., $B_i = B_0$ for rotational and Stokes vibration–rotation lines and $B_i = B_1$ for anti-Stokes vibration–rotation lines. $Q \approx k_B T / 2hc_0 B_0$ is the state sum or partition function. N_2 and O_2 have nuclear spins of $I = 1$ and $I = 0$, respectively, which leads to different nuclear spin statistics. In addition, for homonuclear molecules g_N depends on the initial rotational state J, and we obtain for N_2

$$g_N = \begin{cases} 6 \text{ for } J \text{ even} \\ 3 \text{ for } J \text{ odd} \end{cases} \tag{9.14}$$

and for O_2

$$g_N = \begin{cases} 0 \text{ for } J \text{ even} \\ 1 \text{ for } J \text{ odd.} \end{cases} \tag{9.15}$$

From this condition it follows that every second Raman line of O_2 is missing and that the Raman lines of N_2 show an alternating intensity. The function Φ_J contains the Placzek–Teller factors, the degeneracy

$2J + 1$, and the factor with the molecular constants for the specific observational geometry. In our case (see remark 2) we have to insert for Stokes rotational lines

$$\Phi_J = \frac{7(J+1)(J+2)}{30(2J+3)}\gamma^2, \quad J = 0, 1, 2, \ldots , \tag{9.16}$$

for anti-Stokes rotational lines

$$\Phi_J = \frac{7J(J-1)}{30(2J-1)}\gamma^2, \quad J = 2, 3, 4, \ldots , \tag{9.17}$$

for Stokes vibration–rotation lines of the Q branch

$$\Phi_J = \frac{b_v^2(2J+1)}{[1-\exp(-hc_0\tilde{\nu}_{\mathrm{vib}}/k_{\mathrm{B}}T)]}\left[a'^2 + \frac{7J(J+1)}{45(2J+3)(2J-1)}\gamma'^2\right], \quad J = 0, 1, 2, \ldots , \tag{9.18}$$

for Stokes vibration–rotation lines of the O branch

$$\Phi_J = \frac{b_v^2}{[1-\exp(-hc_0\tilde{\nu}_{\mathrm{vib}}/k_{\mathrm{B}}T)]}\frac{7J(J-1)}{30(2J-1)}\gamma'^2, \quad J = 2, 3, 4, \ldots , \tag{9.19}$$

and for Stokes vibration–rotation lines of the S branch

$$\Phi_J = \frac{b_v^2}{[1-\exp(-hc_0\tilde{\nu}_{\mathrm{vib}}/k_{\mathrm{B}}T)]}\frac{7(J+1)(J+2)}{30(2J+3)}\gamma'^2, \quad J = 0, 1, 2, \ldots . \tag{9.20}$$

In Eqs. (9.13)–(9.20) J is the rotational quantum number of the initial state. Some authors prefer to use the rotational quantum number J'' of the lower energy level involved in the transition instead, which leads to a modification of the equations for anti-Stokes transitions. The latter notation has the advantage that rotational lines of the Stokes and anti-Stokes branches which have the same absolute frequency shifts, i.e., which are symmetric in the spectrum with respect to $\tilde{\nu}_1$, are identified by the same J number.

5) The constants a^2, γ^2, a'^2, and γ'^2 have been determined from different experimental and theoretical approaches for various molecular species. Using values from the literature, one has to be careful as to the specific definition of the polarizability properties (relations are given in Ref. [53], p. 126–127). In older literature, cgs units are used, and the

values have to be either multiplied by $(4\pi\epsilon_0)^2$ before they can be used in the equations given above or the constant $k_{\tilde{\nu}}$ in the equations has to be replaced by $(2\pi)^4$. The molecular constants show a slight dispersion, i.e., they depend on the wavelength of the incident radiation. For a^2 the dispersion can be calculated from the corresponding dispersion of the refractive index n, since

$$a = \frac{2\epsilon_0(n-1)}{N}, \tag{9.21}$$

with the molecule number density N. We find that a^2 decreases by about 5–10% if the incident wavelength increases from 300 to 600 nm, i.e., the dispersion is of the order of 10^{-3} to $10^{-4}\,\mathrm{nm}^{-1}$ and thus negligible for our applications. The same holds for the other constants [63, 64]. Table 9.3 summarizes the molecular constants for the calculation of Raman scattering cross sections of nitrogen and oxygen obtained experimentally at wavelengths between 400 and 500 nm [63, 65, 66]. The factor $(4\pi\epsilon_0)^2$ is indicated separately in order to show the original numbers from the literature.

The third atmospheric molecule of interest, H_2O, is a nonlinear, asymmetric top molecule and the calculation of its Raman spectrum is much more complicated. A recent paper [67] deals with the calculation of the vibration–rotation Raman scattering cross sections of H_2O that follow from the symmetric and antisymmetric O–H stretching vibrations. A table with the molecular constants for more than 7000 vibration–rotation transitions is given. These data were used in the calculation of an atmospheric backscatter spectrum shown in Fig. 9.2 for an incident wavelength of 355 nm. For Rayleigh scattering and for nitrogen and oxygen Raman scattering the positions and intensities of the lines were calculated from the equations given above. In addition, the Raman bands of liquid water and ice are shown in Fig. 9.2 on an arbitrary intensity scale [68–70].

Table 9.3. Molecular constants for the calculation of Raman scattering cross sections of nitrogen and oxygen

Gas	a^2 $\mathrm{m}^6/(4\pi\epsilon_0)^2$	γ^2 $\mathrm{m}^6/(4\pi\epsilon_0)^2$	a'^2 $\mathrm{m}^4/\mathrm{kg}/(4\pi\epsilon_0)^2$	γ'^2 $\mathrm{m}^4/\mathrm{kg}/(4\pi\epsilon_0)^2$
N_2	3.17×10^{-60}	0.52×10^{-60}	2.62×10^{-14}	4.23×10^{-14}
O_2	2.66×10^{-60}	1.26×10^{-60}	1.63×10^{-14}	6.46×10^{-14}

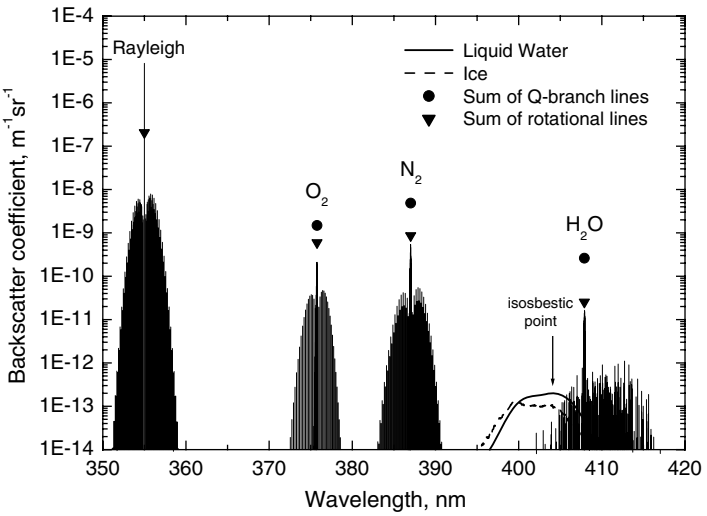

Fig. 9.2. Raman backscatter spectrum of the atmosphere for an incident laser wavelength of 355 nm, normal pressure, a temperature of 300 K, an N_2 and O_2 content of 0.781 and 0.209, respectively, and a water-vapor mixing ratio of 10 g/kg. The curves for liquid water and ice are arbitrarily scaled. The isosbestic point is discussed in Subsection 9.5.2.

9.3 Technical Requirements

The low intensity of the Raman backscatter signals calls for a specific technical lidar setup. A high-power laser transmitter and a highly efficient receiving and detection system are required. Figure 9.3 shows schematically the setup of an aerosol and water-vapor Raman lidar with one emitted wavelength. The lidar consists of a laser, a beam-expanding and transmitter optics, a receiver telescope with field stop, three detection channels for the measurement of the water-vapor and nitrogen Raman signals and the elastic signal, and a data-acquisition and computer unit. The specific requirements for each of the components are explained in the following.

9.3.1 Laser

As mentioned previously, the Raman lidar technique does not require specific emission wavelengths or high spectral purity of the emitted laser light, but a high average laser power and a preferred emission wavelength between 320 and 550 nm. In the beginning of atmospheric Raman lidar observations the nitrogen laser at 337 nm and the ruby laser

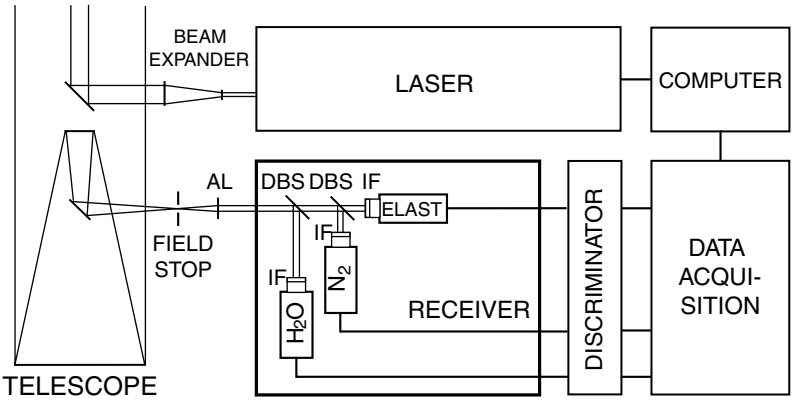

Fig. 9.3. Typical setup of a water-vapor and aerosol Raman lidar. AL – achromatic lens, IF – interference filter, DBS – dichroic beam splitter.

at its fundamental of 694 nm or frequency-doubled to 347 nm were used [1–6, 71]. Because of the relatively low average power of these lasers, early atmospheric Raman measurements were limited to ranges of about 2 km. Pulsed lasers with high average power in the visible and ultraviolet spectral region became available during the 1980s. UV excimer lasers, i.e., XeCl and XeF lasers at 308 and 351 nm, and frequency-tripled Nd:YAG lasers at 355 nm were used first to obtain Raman scattering up to the middle [72] and upper troposphere [9, 10, 73, 74]. Nowadays, the Nd:YAG laser is the workhorse in the Raman lidar field [11, 13, 16, 75–77]. Its primary wavelength of 1064 nm is converted to 532 and 355 nm by frequency-doubling and frequency-tripling techniques. Laser pulse repetition rates of 20 to 50 s^{-1} and pulse energies of 0.5 to 1.5 J at the primary wavelength, resulting in an average power >10 W, are typically used. For the same average power, a higher pulse energy at a lower pulse repetition rate is to be preferred because the signal-to-noise ratio of the measurements, especially at daytime, is improved in this way.

9.3.2 Beam Expander

The typical laser beam divergence of $\sim$1 mrad must be reduced by appropriate beam expansion in order to allow for a narrow telescope field of view, which again will help to suppress background light and thus increase the signal-to-noise ratio. Beam expansion by a factor n reduces the divergence by the same factor. A typical beam-expansion factor is $n = 10$. Reduction of the divergence to less than 0.1 mrad does

not further improve the characteristics of ground-based systems because turbulence in the lower troposphere leads to an effective beam divergence of about that figure.

Mirror or lens telescopes can be used as beam expanders. A laser surface coating for high reflectivity at the emission wavelength in the case of the mirror reflectors is necessary. Lenses need an anti-reflection coating to avoid back-reflection from the surfaces into the laser cavity. Achromatic optics is necessary if light is emitted at more than one wavelength.

9.3.3 Telescope

Receiver telescopes of diameters of the order of 0.5–1 m are typically used in Raman lidar systems. Different configurations, mainly of Cassegrainian type, with ratios of effective focal length to primary aperture of $f/(3 \ldots 6)$, are applied [9, 10, 13, 76]. Coaxial (laser beam is on the optical axis of the telescope) as well as biaxial setups (laser beam is off the optical axis of the telescope and possibly tilted against it) are realized. A field stop in the focal point of the telescope determines the receiver field of view (RFOV). The RFOV is normally a factor of 2–10 larger than the laser beam divergence. A compromise must be found between a small RFOV necessary for high background suppression and a larger RFOV for stable adjustment of the laser beam within the RFOV and for a sufficient signal intensity from short distances.

In the telescope design care must be taken concerning the laser-beam RFOV overlap factor, which is influenced by the laser beam divergence, the RFOV, the imaging properties of the telescope (depth of focus), geometric shadows of the secondary mirror and of mountings within the RFOV, and the relative tilt angle between the laser beam and the optical axis of the telescope. For Raman measurements of water vapor and other gases, particle backscatter coefficient, or temperature, which are calculated from a signal ratio (see Section 9.4 and Chapters 4 and 10), it is sufficient to realize equivalent optical paths of the two signals in the receiver, because then the overlap factor cancels out. Extinction profiling requires an overlap factor of 1 or the exact knowledge of the overlap factor *vs* distance, which is often not given at short range up to 1 km distance from the lidar [78]. Therefore, in high-performance systems a second, small-diameter telescope with larger RFOV is used to cover the near range. The use of a separate near-field telescope helps to keep the large telescope optimized for good background suppression. In addition,

the dynamic range of the system is increased because the lidar signal is divided into a short-range and a long-range part. The shortcoming of this approach is that a second receiver chain has to be implemented which increases complexity and cost of the system.

9.3.4 Receiver Optics

The receiver optics behind the telescope must be optimized for high transmission of the Raman signals. In addition, elastically backscattered light in the Raman channels must be suppressed. In the setup shown in Fig. 9.3 a suppression factor of 10^8 and 10^{10} is necessary in the vibration–rotation nitrogen and water-vapor Raman channels, respectively. Dichroic beam splitters and interference filters are mainly used for this purpose [11, 13, 16, 76]. Dichroic beam splitters reflect light of a certain wavelength range with high efficiency whereas they transmit light of other spectral regions. Interference filters with a bandwidth of <0.5 nm, a peak transmission of 50–70% , and an excellent out-of-band suppression have become available during the past decade. They are one of the reasons why nowadays the Raman lidar technique turns out to be very stable and robust and a good candidate for routine and automated observations.

Grating monochromators can be applied for the wavelength separation as well, especially if high spectral resolution is required as in the case of Raman temperature measurements (see Chapter 10). A double-grating setup or a combination of a grating with filters is necessary to sufficiently suppress the elastically scattered light [16, 37].

9.3.5 Detectors and Data Acquisition

Photomultipliers in photon-counting mode are typically used in Raman lidar systems. High quantum efficiency and low noise are required. In the ultraviolet region, a quantum efficiency of 25% and a dark count rate of $<5\,\mathrm{s}^{-1}$ can be achieved. The detector output pulses can be pre-amplified before discrimination and registration. Counters on the basis of multichannel scalers are used to acquire the signals. To start data acquisition precisely at the time when the laser pulse enters the atmosphere, a trigger signal from a detector (fast photodiode) that senses a fraction of the outgoing pulse can be used. The typical time resolution or window length of data acquisition is $\sim$100 ns which corresponds to a range resolution of 15 m. Typical averaging time for the raw signals is 10–30 s.

(The signals are usually further averaged in time and space during data evaluation.) The number of counts per range gate and unit time is finally stored on a computer.

The whole detector chain from the photomultiplier to the data acquisition system should allow for count rates $\geq$250 MHz or a dead time of $\leq$4 ns. Then, assuming Poisson statistics for the temporal distribution of backscattered photons, dead-time effects will not significantly influence count rates $\leq$10 MHz. Therefore, the maximum count rate must be limited to about that figure by appropriate signal reduction, e.g., by inserting neutral-density filters. Dead-time correction is possible up to about 80 MHz, if the dead-time behavior of the system is exactly known [79, 80]. Under daylight conditions and in the near range, the Raman signals allow analog detection as well. A combination of analog and photon-counting detection can help to increase the system's dynamic range [47].

9.4 Measurement of Water Vapor

In the following, we describe the data evaluation procedure for Raman measurements of gas concentrations. In principle, this procedure is valid for the measurement of any Raman-active gas with sufficiently high atmospheric concentration. As mentioned in the Introduction, we will focus the discussion on the detection of water vapor as the most important observable in this context.

9.4.1 Mixing Ratio

The Raman signal $P_\mathrm{R}(z)$ from distance z measured with lidar at the Raman wavelength λ_R is described by the Raman lidar equation, which can be written as

$$P_\mathrm{R}(z) = \frac{K_\mathrm{R} O(z)}{z^2} \beta_\mathrm{R}(z) \exp\left\{ -\int_0^z [\alpha_0(\zeta) + \alpha_\mathrm{R}(\zeta)] \mathrm{d}\zeta \right\}. \qquad (9.22)$$

$O(z)$ is the factor describing the overlap between the laser beam and the RFOV and is equal to 1 for heights above which the laser beam is completely imaged onto the photomultiplier cathode. K_R comprises all range-independent system parameters such as telescope area, receiver transmission and detection efficiency. β_R is the Raman backscatter cross section, and $\alpha_0(z)$ and $\alpha_\mathrm{R}(z)$ describe the extinction of light on the way

from the lidar to the backscatter region and on the way back to the lidar after the Raman scattering process, respectively. The latter two parameters include light extinction due to Rayleigh scattering and to scattering and absorption by aerosol particles. Molecular absorption can also contribute to this term (see Subsection 9.5.1). The Raman lidar equation (9.22) differs from the usual lidar equation (see Chapter 1) only in the way that 1) the Raman backscatter coefficient

$$\beta_{\mathrm{R}} = N_{\mathrm{R}}(z)\frac{\mathrm{d}\sigma(\pi)}{\mathrm{d}\Omega} \tag{9.23}$$

is given by the molecule number density $N_{\mathrm{R}}(z)$ of the Raman-active gas and the differential Raman cross section for the backward direction $\mathrm{d}\sigma(\pi)/\mathrm{d}\Omega$ (see Section 9.2) and that 2) light extinction on the way back from the scattering volume must be considered at the Raman-shifted wavelength λ_{R}. Depending on the spectral resolution of the receiver, β_{R} and thus $P_{\mathrm{R}}(z)$ can describe the scattering according to a single Raman line, a group of lines, or a whole rotational or vibration–rotation Raman band (see Section 9.2).

The Raman method for gas-concentration measurements, e.g., of water vapor, makes use of two Raman signals, one of which is the return signal P_{R} from the gas of interest, usually the Stokes vibration–rotation Raman band or a part of it, and the other one is the signal P_{Ref} of a reference gas. The Stokes vibration-rotation Raman band of N_2 is typically used as the reference signal. However, the pure rotational Raman band of N_2 and/or O_2 can serve for this purpose as well, if a temperature-insensitive part of the band is chosen and elastic scattering is suppressed sufficiently well [49].

By forming the signal ratio $P_{\mathrm{R}}/P_{\mathrm{Ref}}$ and rearranging the resulting equation, we obtain the mixing ratio of the gas relative to dry air:

$$m(z) = C\frac{P_{\mathrm{R}}(z)}{P_{\mathrm{Ref}}(z)}\frac{\exp[-\int_0^z \alpha_{\mathrm{Ref}}(\zeta)\mathrm{d}\zeta]}{\exp[-\int_0^z \alpha_{\mathrm{R}}(\zeta)\mathrm{d}\zeta]}, \tag{9.24}$$

with the calibration constant C. Equation (9.24) assumes identical overlap factors and range-independent Raman backscatter cross sections for the two signals. The difference between the atmospheric transmission at λ_{R} and the one at λ_{Ref} is mainly caused by Rayleigh scattering and can easily be corrected by using standard atmosphere profiles of temperature and pressure, or, if available, actual radiosonde data. The meteorological data yield the molecule number density. The Rayleigh scattering cross

sections are constant and taken from the literature [81]. Differences in the transmissions at the two Raman wavelengths caused by wavelength-dependent particle extinction are found to be negligible in most cases (see Subsection 9.4.3).

9.4.2 Calibration

Equation (9.24) requires the calibration of the relative measure of the gas concentration. The calibration constant C accounts for the ratio $M_{\mathrm{R}}/M_{\mathrm{air}}$ of the molecule masses of the investigated gas and of air, for the ratio $N_{\mathrm{Ref}}/N_{\mathrm{air}}$ of the molecule number densities of the reference gas and of air, for the transmission and detection efficiency ratio of the lidar system for the two signals, and for the ratio of the *effective* Raman backscatter cross sections of the two gases. We introduce the term *effective* cross section because, particularly when using narrow-bandwidth filters for the selection of the Raman signals, we have to take the average cross section over the spectrum of the observed Raman band, weighted with the instrument's transmission function. In this context we also have to consider a possible temperature, and thus range, dependence of the calibration constant due to a temperature dependence of the signal intensity distribution in the wings of the Raman bands [82, 83].

The calibration constant can be determined in different ways. Most often the lidar measurement is calibrated against an *in situ* observation of the same quantity. In the case of water vapor, it is usually the measurement of the mixing-ratio profile with an accompanying radiosonde. This procedure makes the lidar measurement dependent on the measurement accuracy of a second instrument. The accuracy of lidar calibration with radiosondes has been discussed extensively in the literature. We refer to Ref. [82] for an overview. Several other attempts have been made to develop calibration methods especially for water-vapor observations. For example, the calibration of the range-integrated profile against an atmospheric column value measured with a microwave radiometer has been suggested [84].

In principle, an independent calibration of the system is possible by measuring or calculating the relevant system parameters. The use of two identical filters to obtain nitrogen Raman scattering in both channels can help to estimate their transmission efficiency ratio [85]. Sherlock et al. [82] used diffuse daylight to determine the transmission ratio of the two instrument channels and calculated the ratio of the effective cross sections. The system's short-term and long-term stability together

with the uncertainties inherent in any of the calibration methods lead to the conclusion that calibration errors remain on the order of 5% in any case [82].

9.4.3 Errors

Statistical Errors

The error of Raman lidar measurements is usually dominated by statistical noise. We can assume that the detected photons follow a Poisson distribution, so that the statistical error $\Delta P_i = \sqrt{P_i}$ of each signal is calculated from the number of acquired photon counts P_i, with $i = \mathrm{R}$, Ref. Each signal is the sum of counts from detected Raman-backscattered photons and from sky background photons and electronic noise. The background signal is usually determined at the far end of the lidar range from which no Raman backscattered photons are detected any more, and then subtracted. Both signal noise and background noise contribute to the statistical error of the mixing ratio, which is obtained by applying the law of error propagation to Eq. (9.24).

The achievable measurement accuracy in Raman lidar depends primarily on the system parameters (laser power, telescope diameter), but also on the actual measurement conditions (gas concentration, aerosol extinction). Signals ought to be averaged in time and space until the signal error is $<20\%$ before the data evaluation procedures are applied and total errors are calculated according to the rules of error propagation.

Systematic Errors

Systematic errors mainly arise from the calibration procedure as discussed before. If an accompanying radiosonde is used for calibration, the calibration error can be estimated, e.g., by calculating the standard deviation of the calibration constant from a fit of the relative mixing ratio ($C = 1$) to the radiosonde profile over a certain height range (see Subsection 9.4.4). Furthermore, the variation of the calibration constant by using multiple sondes at different times can be investigated.

As mentioned before, the possible temperature dependence of the effective Raman backscatter cross sections due to narrow filter bandwidths and the resulting altitude dependence of the calibration factor should be investigated for each individual lidar system. Whiteman [80]

found a change in the water-vapor backscatter cross section of 7% for a filter bandwidth of 0.34 nm and a temperature variation between 200 and 300 K.

Other systematic errors follow from the correction of the differential atmospheric transmission for the two signals because of the different extinction on the way back from the scattering volume to the lidar system [exponential terms in Eq. (9.24)]. The correction of Rayleigh scattering is straightforward as already mentioned and errors due to an uncertainty in the applied temperature and pressure profiles are negligible, even if no accompanying radiosonde measurement is available and standard-atmosphere conditions are assumed.

Differential aerosol extinction plays a role for large aerosol optical depths only. The extinction profile is determined from the Raman reference profile for heights for which the overlap factor is 1 or an overlap correction can be applied (see [42, 78] and Chapter 4). For lower heights a linear extrapolation of the extinction profile can be used. For the calculation of the differential aerosol extinction a parameter k, which accounts for the wavelength dependence of aerosol extinction, must be assumed. This parameter, in the literature often referred to as the Ångström exponent and defined as $k = \ln(\alpha_1/\alpha_2)/\ln(\lambda_2/\lambda_1)$, with the extinction coefficients α_1 and α_2 at the wavelengths λ_1 and λ_2, respectively, may vary typically between 0 for marine aerosol or large dust particles and 2 for small industrial pollution particles. Airmass characterization may thus help to estimate k. However, if $k = 1$ is assumed in general and the true k is 0 or 2, the resulting error of the mixing ratio from the transmission correction is $<3\%$ for aerosol optical depths <0.5. The error may reach values up to 10% if the aerosol optical depth is as high as 2 [9, 16, 86]. Advanced Raman lidar systems measure aerosol extinction at more than one wavelength simultaneously, so that the Ångström exponent can even be determined with the same system [87, 88].

Differential ozone absorption must be considered in the transmission correction for laser wavelengths <300 nm only. If, e.g., the XeCl excimer laser at 308 nm is used for water-vapor measurements, the detection wavelengths for water vapor and nitrogen are at 347 and 332 nm, respectively, and the resulting error by neglecting differential ozone absorption is $<1\%$ [86]. In the solar-blind region, the accompanying measurement of ozone profiles, e.g., by applying the ozone Raman DIAL technique (see Subsection 9.5.1) is advisable.

9.4.4 Example

Figure 9.4 shows an example of a water-vapor measurement. The measurement was made with the Raman lidar of the Institute for Tropospheric Research, Leipzig, Germany, on April 23, 2002, between 1930 and 2132 UTC [16]. The mixing-ratio profile was calibrated against the profile from a Vaisala RS-80 radiosonde launched at 2010 UTC at the lidar site. The calibration constant was determined in the height range from 0 to 6.5 km as 0.00877 ± 0.00054, i.e., with an error of about 6%. The right panel of Fig. 9.4 shows the variability of the calibration constant which is mainly attributed to the atmospheric variability during the time of the measurement. The variations are highest in the lower 4 km of the atmosphere. Above 6.5 km the typical underestimation of the water-vapor content for temperatures $<-40°$C with the radiosonde can be seen. This height range was excluded from the calibration. Mixing ratios >1 g/kg are shown on a linear, those <1 g/kg on a logarithmic scale in the left panel of Fig. 9.4. The Raman measurements of the water-vapor mixing ratio typically cover values over three orders of magnitude. The error bars in the figure account for statistical noise and the systematic calibration error.

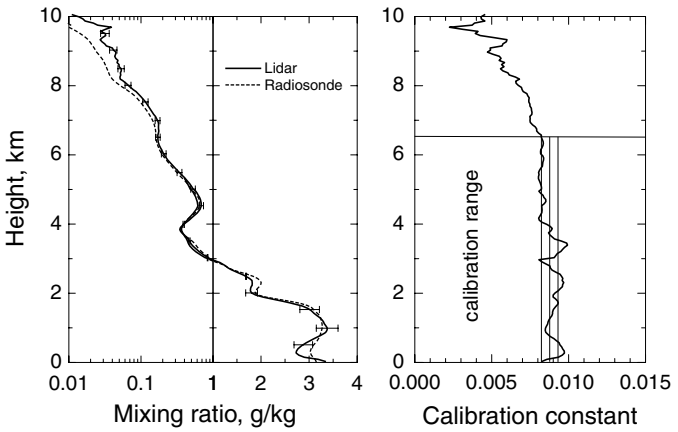

Fig. 9.4. Left: Water-vapor mixing-ratio profile determined with Raman lidar and an accompanying radiosonde. The temporal resolution of the lidar measurement is 2 h, the spatial resolution is 120 m from 0 to 3 km, 480 m from 3 to 5 km and 1200 m above. Right: Calibration constant defined as the ratio of the water-vapor mixing ratio determined with radiosonde and the one obtained with the uncalibrated lidar [$C = 1$ in Eq. (9.24)], mean value and standard deviation for the height range 0–6.5 km.

9.5 Other Applications

9.5.1 Ozone Raman DIAL

Ozone Raman DIAL is based on the differential-absorption lidar or DIAL method, i.e., it makes use of two backscatter signals one of which is more strongly absorbed by ozone than the other (see Chapter 7). Unlike in conventional DIAL, the two signals are not elastically backscattered by molecules and particles, but Raman backscattered by molecules of nitrogen and/or oxygen alone. The advantage of Raman DIAL against conventional DIAL is that the error term due to differential backscattering disappears. Conventional DIAL ozone measurements in regions with inhomogeneous aerosol load are hard to carry out because of this error, particularly if the two wavelengths are separated widely as it is the case for stratospheric lidar systems and also for many tropospheric systems working in the solar-blind region.

After the eruption of Mt. Pinatubo in 1991, the stratosphere was globally contaminated with sulfuric-acid particles for several years and the conventional stratospheric ozone DIAL method could not be applied any more. At that time McGee et al. [44, 89] suggested using two nitrogen Raman signals for the measurement of differential ozone absorption. They used two laser wavelengths of a conventional DIAL system, 308 nm from a XeCl laser and 351 nm from a XeF laser, and measured the Stokes vibration–rotation nitrogen Raman bands at 332 and 382 nm as the on-line and off-line signals, respectively. With a combination of a XeCl and a frequency-tripled Nd:YAG laser (355 nm; N_2 VRR at 387 nm) Reichardt et al. [45, 90] applied the technique to the measurement of ozone in cirrus clouds. Later, Reichardt et al. [46] showed that the method also works with a single XeCl laser, if the pure rotational signal of nitrogen and oxygen is used in conjunction with a vibration–rotation Raman band of oxygen or nitrogen. They called this technique RVR Raman DIAL. This approach not only reduces the complexity of the lidar system, but the sensitivity of the Raman DIAL method to multiple scattering effects in clouds as well [91], because of the smaller wavelength difference between the on- and the off-line signal.

Figure 9.5 shows the ozone absorption cross section in the 250-to-350-nm spectral region of the Hartley band [92] together with the wavelengths $\lambda > 300$ nm used for the ozone Raman DIAL measurements in the upper troposphere and stratosphere described above. Also shown are wavelengths that can be used for ozone Raman DIAL applications in

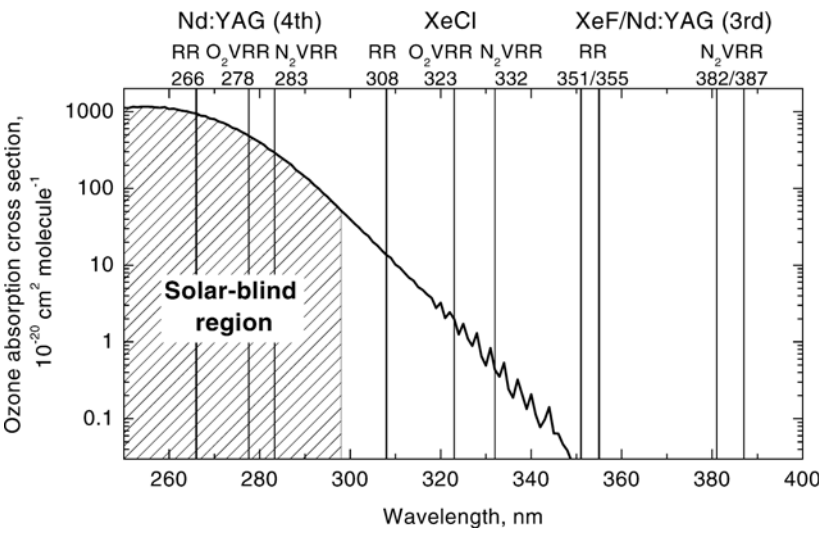

Fig. 9.5. Ozone absorption cross section and wavelengths applied in the ozone Raman DIAL technique for upper tropospheric and stratospheric measurements ($\lambda > 300$ nm) and for boundary-layer measurements in the solar-blind region ($\lambda < 300$ nm).

the solar-blind region (shaded area). The fourth harmonic of the Nd:YAG laser is a typical laser source here and the vibration–rotation Raman lines of oxygen and nitrogen at 278 and 283 nm are then the on-line and off-line signals, respectively. Measurements of ozone concentrations in the planetary boundary layer up to about 2 km height can be made with this technique independent of the time of the day [29, 93, 94].

The two reference signals used in the Raman DIAL method may be written as $P_{\mathrm{Ref}}^{\mathrm{on}}$ and $P_{\mathrm{Ref}}^{\mathrm{off}}$. By differentiation of the logarithm of the ratio of these two signals, we obtain the ozone molecule number density

$$N_{\mathrm{O_3}}(z) = \frac{1}{\Delta\sigma_{\mathrm{abs}}(T)} \left(\frac{\mathrm{d}}{\mathrm{d}z} \ln \frac{P_{\mathrm{Ref}}^{\mathrm{on}}(z)}{P_{\mathrm{Ref}}^{\mathrm{off}}(z)} - \Delta\alpha_{\mathrm{aer}}(z) - \Delta\alpha_{\mathrm{mol}}(z) \right). \tag{9.25}$$

Here we must consider the extinction because of ozone absorption, $\alpha_{\mathrm{abs}} = N_{\mathrm{O_3}}\sigma_{\mathrm{abs}}$, with the ozone absorption cross section σ_{abs}, in the exponential term of the Raman lidar equation (9.22). The ozone absorption cross section σ_{abs} is a function of temperature and therefore depends on height z. For a Raman DIAL system with two emission wavelengths, the three Δ expressions consist of four terms each,

$$\Delta\xi = \xi(\lambda_0^{\mathrm{on}}) + \xi(\lambda_{\mathrm{R}}^{\mathrm{on}}) - \xi(\lambda_0^{\mathrm{off}}) - \xi(\lambda_{\mathrm{R}}^{\mathrm{off}}), \tag{9.26}$$

with $\xi = \sigma_{\mathrm{abs}}$, α_{mol}, α_{aer}. λ_0^{on} and λ_0^{off} are the laser wavelengths and $\lambda_{\mathrm{R}}^{\mathrm{on}}$ and $\lambda_{\mathrm{R}}^{\mathrm{off}}$ the wavelengths of the vibration–rotation bands. For RVR Raman DIAL the equation reduces to

$$\Delta\xi = \xi(\lambda_{\mathrm{R}}^{\mathrm{on}}) - \xi(\lambda_{\mathrm{R}}^{\mathrm{off}}), \tag{9.27}$$

with the wavelengths $\lambda_{\mathrm{R}}^{\mathrm{on}}$ and $\lambda_{\mathrm{R}}^{\mathrm{off}}$ of the pure rotational and the vibration–rotation band, respectively.

The calculation of the differential Rayleigh scattering and the differential aerosol extinction is done in the same way as discussed in Subsection 9.4.3 for water vapor, i.e., Rayleigh scattering is calculated from temperature and pressure profiles and aerosol extinction is determined from the Raman signal which is less influenced by ozone under the assumption of an Ångström exponent for the wavelength dependence.

9.5.2 Measurement of Liquid Water

Raman signals from liquid water droplets in clouds have been first obtained as an enhanced water-vapor Raman signal corresponding to more than 100% relative humidity [34]. Because the measurements were done with a XeF excimer laser, which has several emission lines in the 348-to-353-nm region, and with relatively broad interference filters of 7–8 nm bandwidth, a considerable part of the liquid-water Raman band shown in Fig. 9.2 was detected in the water-vapor channel and led to an increased signal within the cloud. Demoz et al. [95] used the enhanced water-vapor Raman signal for the determination of cloud base height during light rain and cloud virga conditions, when other methods based on elastic backscattering gave questionable results. Whiteman and Melfi [35] suggested using the Raman signal from liquid water together with the elastic backscatter signal to determine liquid-water content, droplet radius, and droplet number density at the base of tropospheric clouds (the penetration depth is typically of the order of 100–200 m for optically dense water clouds).

For the determination of the liquid-water content from the Raman signal several requirements must be fulfilled. First of all, there must be proportionality between the Raman signal intensity and the liquid-water content. For single water droplets this condition is not met, since the Raman scattering cross section shows a variety of resonances with properties that depend on droplet size [96, 97]. However, the size distribution of cloud droplets is normally broad, and by integration over a range of sizes the cross section is found to be proportional to the droplet

volume [35, 97]. Second, an appropriate separation of the liquid-water Raman signal from the signal of water vapor is necessary. Because the two spectra overlap, the measurements must be carried out with high spectral resolution. Arshinov et al. [36] used a seeded Nd:YAG laser and a 32-channel receiving system to resolve the Raman spectrum between 3000 and 4200 cm^{-1} frequency shift. A double-grating monochromator together with a holographic notch filter allowed a suppression of elastic scattering by 14 orders of magnitude. The photocathode of a 32-anode Hamamatsu photomultiplier was placed in the imaging plane of the spectrometer. In this way, spectrally resolved lidar signals could be measured in 32 channels simultaneously, and water-vapor and liquid-water signals could be separated.

The final point of interest is the sensitivity of the liquid-water backscatter spectrum to temperature. Whiteman et al. [98] showed that an isosbestic, i.e., a nearly temperature-insensitive, point in the liquid-water spectrum exists at a shift of 3425 cm^{-1} (see Fig. 9.2). Thus, narrow-bandwidth detection of the liquid-water signal at that frequency will allow temperature-insensitive measurements.

The studies on the measurement of liquid water mentioned here represent an ongoing research. We can expect further results and new developments in the future.

9.6 Concluding Remarks

Nowadays, Raman lidar systems are instruments widely applied in atmospheric research with focus on water vapor, temperature (see Chapter 10), ozone, aerosols, and optically thin clouds (see Chapter 4). Because of their stable and robust setup, they are especially suitable for routine, automated, long-term atmospheric observations. The comparably small Raman scattering cross sections and the resulting low signal-to-noise ratios require appropriate temporal and spatial Raman signal averaging. The typical resolution of Raman measurements is 1–30 minutes in time and 50–300 m in space in the lower troposphere and 10 minutes to 2 h in time and 0.3–2 km in space in the upper troposphere and lower stratosphere. Raman lidar instruments are therefore used in climate and weather research to provide statistically significant information on the atmosphere, to establish climatologies of aerosols and water vapor [14, 15, 99], and to study mesoscale and large-scale processes such as frontal passages [100], hurricanes [101], and long-range

transport [16, 88, 102]. In the near range up to a few hundred meters distance and under a horizontal measurement geometry, water-vapor measurements for the study of turbulent fluxes were even made with a resolution of 1.5 m and 0.8 s [103].

Advanced Raman lidar systems are multichannel, multipurpose instruments which combine several Raman techniques and take measurements at several wavelengths [13, 16]. The characterization of the atmosphere in terms of the most important meteorological quantities, i.e., temperature and humidity, a comprehensive characterization of aerosol properties (see Chapter 4), and the investigation of dependencies between the observables, e.g., aerosol properties and relative humidity or ozone concentration and aerosol and cloud particle properties, are possible with such instruments.

A few pioneering steps in the application of Raman lidar systems in routine, long-term atmospheric monitoring may serve as a summarizing illustration of the potential of the technique:

- *Water vapor:* An operational Raman lidar has been working unattended and autonomously at the Cloud and Radiation Testbed site of the Atmospheric Radiation Measurement Program of the U.S. Department of Energy in Oklahoma since 1996. The lidar is one of several instruments in the program, the goal of which is to collect a 10-year data set on water vapor, aerosols, and clouds. The Raman lidar system is delivering the first long-term water-vapor climatology based on lidar measurements [11, 14, 99].
- *Ozone:* The Network for the Detection of Stratospheric Change, NDSC, applies lidar instruments to observe stratospheric ozone concentrations on a global scale. The Raman DIAL technique was implemented in these systems after the eruption of Mt. Pinatubo [104–106]. The network has meanwhile established an ozone climatology over more than a decade [107, 108].
- *Stratospheric Aerosol:* The aerosol load in the stratosphere and its decline after the eruption of Mt. Pinatubo in the Philippines in June 1991 had been observed with a Raman lidar for five years [48]. Aerosol extinction and backscatter profiles from Raman lidar measurements could be converted to particle effective radius, mass and surface-area concentrations [109] (see Chapter 4).
- *Tropospheric Aerosol:* The European Aerosol Research Lidar Network EARLINET carried out a three-year routine monitoring of the aerosol conditions over Europe. Out of the 21 stations of

the network, 11 use the Raman lidar technique to acquire aerosol extinction profiles. Several systems measure water vapor simultaneously. EARLINET is the first lidar network on a continental scale and the first network that applied Raman lidar as the basic monitoring technique [15].

The success of these applications will lead to the first Raman lidar system installed by a weather service for routine water-vapor and aerosol observations in the near future [110].

In addition to the well-established Raman lidar techniques mentioned above, there are more new and challenging applications under development. Recently, relative-humidity observations throughout the troposphere have been demonstrated by a combination of the water-vapor and temperature Raman techniques [16]. In conjunction with the spectrally resolved observation of liquid water with a 32-channel system, Arshinov et al. [36] found an unexpected return signal which they interpreted as scattering from water-molecule clusters, an intermediate state of water during transition between the gaseous and the liquid phase. Whiteman et al. [111] studied the feasibility of water-vapor Raman measurements from aircraft and found a reasonable performance. Together with the ongoing research on the measurement of liquid water (see Subsection 9.5.2) these examples may show some of the ways to go in the future for new applications of the lidar technique.

References

[1] D.A. Leonard: Nature **216**, 142 (1967)
[2] J.A. Cooney: Appl. Phys. Lett. **12**, 40 (1968)
[3] J. Cooney, J. Orr, C. Tomasetti: Nature **224**, 1098 (1969)
[4] S.H. Melfi, J.D. Lawrence Jr, M.P. McCormick: Appl. Phys. Lett. **15**, 295 (1969)
[5] J. Cooney: J. Appl. Meteorol. **11**, 108 (1972)
[6] S.H. Melfi: Appl. Opt. **11**, 1605 (1972)
[7] H. Inaba: Detection of atoms and molecules by Raman scattering and resonance fluorescence. In *Laser Monitoring of the Atmosphere*, E.D. Hinkley, ed. (Springer, Berlin 1976), pp. 153–236
[8] W.B. Grant: Opt. Engineer. **30**, 40 (1991)
[9] A. Ansmann, M. Riebesell, U. Wandinger, et al.: Appl. Phys. B **55**, 18 (1992)
[10] D.N. Whiteman, S.H. Melfi, R.A. Ferrare: Appl. Opt. **31**, 3068 (1992)
[11] J.E.M. Goldsmith, F.H. Blair, S.E. Bisson, et al.: Appl. Opt. **37**, 4979 (1998)
[12] R.A. Ferrare, S.H. Melfi, D.N. Whiteman, et al.: J. Geophys. Res. **103**, 19,663 (1998)

[13] D. Althausen, D. Müller, A. Ansmann, et al.: J. Atmos. Oceanic Technol. **17**, 1469 (2000)
[14] D.D. Turner, R.A. Ferrare, L.A. Brasseur: Geophys. Res. Lett. **28**, 4441 (2001)
[15] J. Bösenberg, M. Alpers, A. Ansmann, et al.: In *Lidar Remote Sensing in Atmosphere and Earth Sciences. Reviewed and revised papers presented at the twenty-first International Laser Radar Conference (ILRC21), Québec, Canada, 8–12 July 2002*. L.R. Bissonnette, G. Roy, G. Vallée, eds. (Defence R&D Canada Valcartier, Val-Bélair, QC, Canada), Part 1, p. 293
[16] I. Mattis, A. Ansmann, D. Althausen, et al.: Appl. Opt. **41**, 6451 (2002)
[17] S.E. Bisson, J.E.M. Goldsmith, M.G. Mitchell: Appl. Opt. **38**, 1841 (1999)
[18] Yu.F. Arshinov, S.M. Bobrovnikov: Appl. Opt. **38**, 4635 (1999)
[19] Yu. Arshinov, S. Bobrovnikov, I. Serikov, et al.: In *Advances in Laser Remote Sensing. Selected Papers presented at the 20th International Laser Radar Conference (ILRC), Vichy, France, 10–14 July 2000*. A. Dabas, C. Loth, J. Pelon, eds. (École Polytechnique, Palaiseau, France 2001), p. 121
[20] D. Renaut, J.C. Pourny, R. Capitini: Opt. Lett. **5**, 233 (1980)
[21] K. Petri, A. Salik, J. Cooney: Appl. Opt. **21**, 1212 (1982)
[22] J. Cooney, K. Petri, A. Salik: Appl. Opt. **24**, 104 (1985)
[23] D. Renaut, R. Capitini: J. Atmos. Oceanic Technol. **5**, 585 (1988)
[24] W.E. Eichinger, D.I. Cooper, F.L. Archuletta, et al.: Appl. Opt. **33**, 3923 (1994)
[25] J. Zeyn, W. Lahmann, C. Weitkamp: Opt. Lett. **21**, 1301 (1996)
[26] D. Kim, H. Cha, J. Park, et al.: J. Korean Phys. Soc. **30**, 458 (1997)
[27] W.E. Eichinger, D.I. Cooper, P.R. Forman, et al.: J. Atmos. Oceanic Technol. **16**, 1753 (1999)
[28] F. De Tomasi, M.R. Perrone, M.L. Protopapa: Nuovo Cimento **23**, 587 (2000)
[29] C.R. Philbrick: In *Lidar Remote Sensing in Atmosphere and Earth Sciences. Reviewed and revised papers presented at the twenty-first International Laser Radar Conference (ILRC21), Québec, Canada, 8–12 July 2002*. L.R. Bissonnette, G. Roy, G. Vallée, eds. (Defence R&D Canada Valcartier, Val-Bélair, QC, Canada), Part 2, p. 535
[30] H. Inaba, T. Kobayashi: Opto-Electr. **4**, 101 (1972)
[31] S.K. Poultney, M.L. Brumfield, J.H. Siviter Jr: Appl. Opt. **16**, 3180 (1977)
[32] J.D. Houston, S. Sizgoric, A. Ulitsky, et al.: Appl. Opt. **25**, 2115 (1986)
[33] W.S. Heaps, J. Burris: Appl. Opt. **35**, 7128 (1996)
[34] S.H. Melfi, K.D. Evans, J. Li, et al.: Appl. Opt. **36**, 3551 (1997)
[35] D.N. Whiteman, S.H. Melfi: J. Geophys. Res. **104**, 31,411 (1999)
[36] Yu.F. Arshinov, S.M. Bobrovnikov, A.I. Nadeev, et al.: In *Lidar Remote Sensing in Atmosphere and Earth Sciences. Reviewed and revised papers presented at the twenty-first International Laser Radar Conference (ILRC21), Québec, Canada, 8–12 July 2002*. L.R. Bissonnette, G. Roy, G. Vallée, eds. (Defence R&D Canada Valcartier, Val-Bélair, QC, Canada), Part 1, p. 31
[37] Yu.F. Arshinov, S.M. Bobrovnikov, V.E. Zuev, et al.: Appl. Opt. **22**, 2984 (1983)
[38] D. Nedeljkovic, A. Hauchecorne, M.L. Chanin: IEEE Trans. Geosc. Remote Sens. **31**, 90 (1993)
[39] G. Vaughan, D.P. Wareing, S.J. Pepler, et al.: Appl. Opt. **32**, 2758 (1993)
[40] A. Behrendt, J. Reichardt: Appl. Opt. **39**, 1372 (2000)
[41] D. Kim, H. Cha, J. Lee, et al.: J. Korean Phys. Soc. **39**, 838 (2001)

[42] A. Ansmann, M. Riebesell, C. Weitkamp: Opt. Lett. **15**, 746 (1990)
[43] A. Ansmann, U. Wandinger, M. Riebesell, et al.: Appl. Opt. **31**, 7113 (1992)
[44] T.J. McGee, M. Gross, R. Ferrare, et al.: Geophys. Res. Lett. **20**, 955 (1993)
[45] J. Reichardt, U. Wandinger, M. Serwazi, et al.: Opt. Eng. **5**, 1457 (1996)
[46] J. Reichardt, S.E. Bisson, S. Reichardt, et al.: Appl. Opt. **39**, 6072 (2000)
[47] D.N. Whiteman, K. Evans, B. Demoz, et al.: In *Lidar Remote Sensing in Atmosphere and Earth Sciences. Reviewed and revised papers presented at the twenty-first International Laser Radar Conference (ILRC21), Québec, Canada, 8–12 July 2002*. L.R. Bissonnette, G. Roy, G. Vallée, eds. (Defence R&D Canada Valcartier, Val-Bélair, QC, Canada), Part 2, p. 551
[48] A. Ansmann, I. Mattis, U. Wandinger, et al.: J. Atmos. Sci. **54**, 2630 (1997)
[49] D. Müller, I. Mattis, U. Wandinger, et al.: J. Geophys. Res. **108**, 10.1029/2002JD002918 (2003)
[50] C.V. Raman, K.S. Krishnan: Nature **121**, 501 (1928)
[51] G. Landsberg, L. Mandelstam: Naturwiss. **16**, 557 (1928)
[52] G. Placzek: Rayleigh-Streuung und Raman-Effekt. In *Handbuch der Radiologie*, vol VI, part II, E. Marx, ed. (Akademische Verlagsgesellschaft, Leipzig 1934), pp. 205–374
[53] D.A. Long, *The Raman Effect* (Wiley, New York 2002)
[54] G. Herzberg, *Molecular Spectra and Molecular Structure. I. Spectra of Diatomic Molecules*, 2nd edn (van Nostrand, Toronto 1950)
[55] D.A. Long, *Raman Spectroscopy* (McGraw Hill, New York 1977)
[56] S. Brodersen: High-resolution rotation-vibrational Raman spectroscopy. In *Raman Spectroscopy of Gases and Liquids*, A. Weber, ed. (Springer, Berlin 1979), p. 7
[57] A. Weber: High-resolution rotational Raman spectra of gases. In *Raman Spectroscopy of Gases and Liquids*, A. Weber, ed. (Springer, Berlin 1979), p. 71
[58] R.J. Butcher, D.V. Willetts, W.J. Jones: Proc. R. Soc. London Ser. A **324**, 231 (1971); the exponent 2 should be replaced by 3 in Eq. (8) on p. 238
[59] J. Bendtsen: J. Raman Spectrosc. **2**, 133 (1974)
[60] H.G.M. Edwards, E.A.M. Good, D.A. Long: J. Chem. Soc., Faraday Trans. II **72**, 865 (1976)
[61] M. Loëte, H. Berger: J. Mol. Spectrosc. **68**, 317 (1977)
[62] T. Hirschfeld: Appl. Spectrosc. **27**, 389 (1973)
[63] G.R. Alms, A.K. Burnham, W.H. Flygare: J. Chem. Phys. **63**, 3321 (1975)
[64] M. Pecul, A. Rizzo: J. Chem. Phys. **116**, 1259 (2002)
[65] M.A. Buldakov, I.I. Matrosov, T.N. Popova: Opt. Spectrosc. **46**, 867 (1979)
[66] W.F. Murphy, W. Holzer, H.J. Bernstein: Appl. Spectrosc. **23**, 211 (1969)
[67] G. Avila, J.M. Fernandez, B. Mate, et al.: J. Mol. Spectrosc. **196**, 77 (1999)
[68] N.P. Romanov, V.S. Shuklin: Opt. Spectrosc. **38**, 1120 (1975)
[69] Z.A. Gabrichidze: Opt. Spectrosc. **19**, 575 (1965)
[70] S.M. Pershin, A.F. Bunkin: Opt. Spectrosc. **85**, 190 (1998)
[71] J.C. Pourny, D. Renaut, A. Orszag: Appl. Opt. **18**, 1441 (1979)
[72] S.H. Melfi, D. Whiteman: Bull. Amer. Meteor. Soc. **66**, 1288 (1985)
[73] J.E.M. Goldsmith, S.E. Bisson, R.A. Ferrare, et al.: Bull. Amer. Meteor. Soc. **75**, 975 (1994)

[74] R.A. Ferrare, S.H. Melfi, D.N. Whiteman, et al.: J. Atmos. Oceanic Technol. **12**, 1177 (1995)
[75] S. Rajan, T.J. Kane, C.R. Philbrick: Geophys. Res. Lett. **21**, 2499 (1994)
[76] V. Sherlock, A. Garnier, A. Hauchecorne, et al.: Appl. Opt. **38**, 5838 (1999)
[77] G. Larchevêque, I. Balin, R. Nessler, et al.: Appl. Opt. **41**, 2781 (2002)
[78] U. Wandinger, A. Ansmann: Appl. Opt. **41**, 511 (2002)
[79] D.P. Donovan, J.A. Whiteway, A.I. Carswell: Appl. Opt. **32**, 6742 (1993)
[80] D.N. Whiteman: Appl. Opt. **42**, 2571 (2003)
[81] A. Bucholtz: Appl. Opt. **34**, 2765 (1995)
[82] V. Sherlock, A. Hauchecorne, J. Lenoble: Appl. Opt. **38**, 5816 (1999)
[83] D.N. Whiteman: Appl. Opt. **42**, 2593 (2003)
[84] D.D. Turner, J.E.M. Goldsmith: J. Atmos. Oceanic. Technol. **16**, 1062 (1999)
[85] G. Vaughan, D.P. Wareing, L. Thomas, et al.: Q. J. R. Meteor. Soc. **114**, 1471 (1988)
[86] A. Ansmann, M. Riebesell, U. Wandinger, et al.: In *Fifteenth International Laser Radar Conference. Abstracts of papers. Tomsk, USSR, July 23–27, 1990*. (Institute of Atmospheric Optics, Tomsk, USSR 1990), Part 1, p. 256
[87] I. Mattis, A. Ansmann, D. Müller, et al.: Geophys. Res. Lett. **29**, 10.1029/2002GL014721 (2002)
[88] K. Franke, A. Ansmann, D. Müller, et al.: J. Geophys. Res. **108**, 10.1029/2002JD002473 (2003)
[89] T.J. McGee, M.R. Gross, U.N. Singh, et al.: Opt. Eng. **34**, 1421 (1995)
[90] J. Reichardt, A. Ansmann, M. Serwazi, et al.: Geophys. Res. Lett. **23**, 1929 (1996)
[91] J. Reichardt: Appl. Opt. **39**, 6058 (2000)
[92] L.T. Molina, M.J. Molina: J. Geophys. Res. **91**, 14,501 (1986)
[93] F. de Tomasi, M.R. Perrone, M.L. Protopapa: Appl. Opt. **40**, 1314 (2001)
[94] B. Lazzarotto, M. Frioud, G. Larchevêque, et al.: Appl. Opt. **40**, 2985 (2001)
[95] B. Demoz, D. Starr, D. Whiteman, et al.: Geophys. Res. Lett. **27**, 1899 (2000)
[96] G. Schweiger: J. Opt. Soc. Am. B **8**, 1770 (1991)
[97] I. Veselovskii, V. Griaznov, A. Kolgotin, et al.: Appl. Opt. **41**, 5783 (2002)
[98] D.N. Whiteman, G.E. Walrafen, W.-H. Yang, et al.: Appl. Opt. **38**, 2614 (1999)
[99] D.D. Turner, R.A. Ferrare, L.A. Heilman Brasseur, et al.: J. Atmos. Oceanic Technol. **19**, 37 (2002)
[100] S.H. Melfi, D. Whiteman, R. Ferrare: J. Appl. Meteorol. **28**, 789 (1989)
[101] D.N. Whiteman, K.D. Evans, B. Demoz, et al.: J. Geophys. Res. **106**, 5211 (2001)
[102] U. Wandinger, D. Müller, C. Böckmann, et al.: J. Geophys. Res. **107**, 10.1029/2000JD00202 (2002)
[103] D.I. Cooper, W.E. Eichinger, D.B. Holtkamp, et al.: Boundary-Layer Meteorol. **61**, 389 (1992)
[104] I.S. McDermid, J.B. Bergwerff, G. Bodeker, et al.: J. Geophys. Res. **103**, 28,683 (1998)
[105] R.D. McPeters, D.J. Hofmann, M. Clark, et al.: J. Geophys. Res. **104**, 30,505 (1999)
[106] W. Steinbrecht, R. Neuber, P. von der Gathen, et al.: J. Geophys. Res. **104**, 30,515 (1999)
[107] E.J. Brinksma, J.B. Bergwerff, G.E. Bodeker, et al.: J. Geophys. Res. **105**, 17,291 (2000)

[108] S. Godin-Beekmann, J. Porteneuve, A. Garnier: J. Environ. Monit. **5**, 57 (2003)
[109] U. Wandinger, A. Ansmann, J. Reichardt, et al.: Appl. Opt. **34**, 8315 (1995)
[110] D. Engelbart: In *Lidar Remote Sensing in Atmosphere and Earth Sciences. Reviewed and revised papers presented at the twenty-first International Laser Radar Conference (ILRC21), Québec, Canada, 8–12 July 2002*. L.R. Bissonnette, G. Roy, G. Vallée, eds. (Defence R&D Canada Valcartier, Val-Bélair, QC, Canada), Part 2, p. 705
[111] D.N. Whiteman, G. Schwemmer, T. Berkhoff, et al.: Appl. Opt. **40**, 375 (2001)